Multicolor-illuminated charge-state dynamics of the nitrogen-vacancy center in diamond

Peng Qian [1,*] Yunpeng Zhai [1] Jun Hu [1] Renfei Zheng,[1] Bing Chen,[1,†] and Nanyang Xu[2,‡]

[1]*School of Physics, Hefei University of Technology, Hefei, Anhui 230009, China*
[2]*Research Center for Quantum Sensing, Zhejiang Lab, Hangzhou 311000, China*

Charge-state conversion has been a very useful tool for improving the performance of nitrogen-vacancy (NV) centers in diamond in many application scenarios. Lasers of different colors are employed to manipulate the NV charge, ranging from blue to infrared. Here, we focus on the study of the charge-state dynamics under illumination of multicolors and their combination with infrared (IR) light, and the results are directly presented in terms of charge-state population. It is shown that each color of light serves some kind of superiority over others in charge-state conversion and a greatly improved conversion rate can be induced by the additional IR illumination. We report that the steady-state NV$^-$ population is increased up to 82% by IR light, and it presents basically the same response trend to infrared power as that of fluorescence counts. We also report a fast-oscillating fluorescence time trace by modulating the IR power. We believe that our work offers some straightforward results that might be of interest to researchers and lead to a clearer understanding of the NV charge-state dynamics.

I. INTRODUCTION

The atomlike defects accommodating spin levels deep within the wide band gap of semiconductors have attracted a growing interest in the community of quantum information [1,2], especially of single-photon emitters [3–5]. Among all the prominent candidates such as defects in diamond [6], silicon carbide [7,8], and hexagonal boron nitride [9,10], the nitrogen vacancy (NV) center in diamond still leads the way due to its long spin coherence time and excellent optical addressability and has been continuously studied for over a decade [11–16]. Although it has long been known that the negatively charged NV center (NV$^-$) which people are usually concerned with can be converted into neutral charge state (NV^0) [17], it was not until recent years that people utilized charge-state conversion (CSC) to develop new fascinating technologies, such as optical nanoscopy [18,19], photoelectrical spin readout [20,21], charge-based memories [22,23], and spin readout via spin-to-charge conversion [24,25]. These improvements greatly promoted the potentials of NV centers in quantum computing and nanoscale sensing [26,27].

In these experiments, illumination at various wavelengths was employed to perform controlled charge conversion and detection, covering from blue to infrared (IR) [28–31]. Each wavelength was used to achieve some specific operation task. However, most of the works only reported information related to one aspect of CSC. In this paper, we concentrate on introducing the general means to manipulate the NV charge state and explicitly measure how the charge population is affected by lasers of different colors. Four typical wavelengths are employed in our experiments, including 532, 594, 637, and 1040 nm. With such different colors, the charge conversion rate at different laser powers are measured. We also observe the charge population altering and fluorescence modulation under the simultaneous excitation with IR and other light. The explanations for the dynamics behind the data are appropriately given.

II. CHARGE STATE CONVERSION AND MEASUREMENT

The experimental setup is shown in Fig. 1(a). A home-built confocal microscopy system is used to address naturally occurring single NV centers in a type-IIa, single-crystal electronic-grade chemical vapor deposition (CVD) bulk diamond (from Element Six, [N] <5 ppb) at room temperature [32]. The NV centers are about 10 microns deep below the surface. Four beams of different wavelengths (solid-state lasers, from Changchun New Industries) are well aligned with dichroic mirrors (DMs) and a RGB combiner fiber (from Thorlabs) which combines green, orange, and red light into one output channel. An oil-immersion microscope objective with 1.45 N.A. (from Olympus) focuses all the light onto the diamond sample while collects single photons reversely. Since the long-pass filter DM2 reflects photons between 650 and 950 nm into the single-photon counting module, which mostly matches the spectral sideband of NV$^-$ rather than NV^0, the recorded fluorescence is mainly attributed to the negative charge. The continuous-wave lasers are gated with acoustooptic modulators to create pulse sequence. The 594-nm laser is attenuated to a very weak level for charge-state detection. Since the zero phonon lines (ZPLs) of NV^0 and NV$^-$ are 575 and 637 nm, respectively, a 532-nm photon has more than enough energy to excite the sidebands of both

*pqian@hfut.edu.cn
†bingchenphysics@hfut.edu.cn
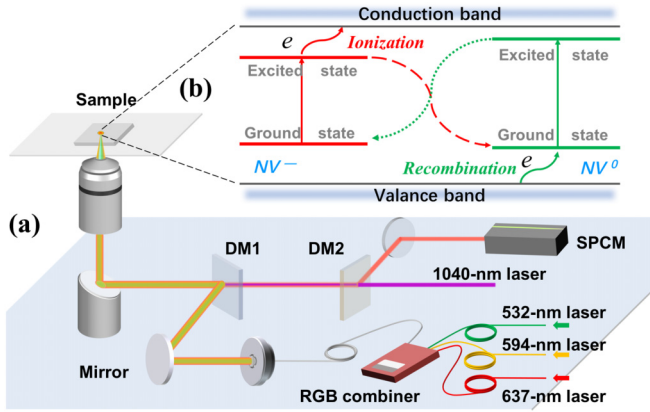‡nyxu@zhejianglab.edu.cn

FIG. 1. (a) Experimental setup. A RGB combiner puts the light of the three colors together into one path. DM1 and DM2 are long-pass dichroic mirrors with edge wavelengths of 650 and 950 nm, respectively. DM2 separates the fluorescence out into the single-photon counting module (SPCM). (b) Diagram of the energy levels and the CSC process of NV centers. The red arrows indicate the conversion from NV^- to NV^0, and the green arrows indicate from NV^0 to NV^-. The two conversion processes are indicated as ionization and recombination, respectively.

charge states strongly, while the 594- and 637-nm photons only pump NV^- efficiently. Therefore, as shown in Fig. 1(b), the light of each of the three colors is capable of converting the center from NV^- to NV^0 through a two-photon process [28,33]: First driving the center from the ground state to the excited state, then exciting one electron into the conduction band (ionization). However, the conversion from NV^0 to NV^- is generally preferred when the center is illuminated by 532-nm light continuously. Following the NV^0 being excited, an extra electron is captured from the valence band (recombination), which results in a maximal NV^- population around 75% in the steady state among various wavelengths [28]. Thus, the distribution of the two charge states depends on the ratio of ionization and recombination rates, and both conversion processes depend quadratically with the illumination power [29,30].

The check of the NV charge is achieved with a technique called single-shot readout, where the number of collected photons in one measurement is used to determine in which charge state the NV center dwells [24,34,35]. Figure 2 displays the statistics for the photon numbers from 5×10^4 measurements, each measurement containing a 15-ms-long 594-nm readout pulse following a long-enough initialization pulse. The statistic is fitted with two Poisson distributions. It is clear that the two charge states can be distinguished with some photon number threshold between the two peaks. In contrast to the near-unit population $99.2 \pm 1.8\%$ of NV^0 initialized with 637-nm laser, the NV^- population initialized with 532-nm laser reaches only $76.7 \pm 0.9\%$. The length of the 594-nm readout pulse should be decided carefully since a short one may not induce enough photons to distinguish the spontaneous emission of two charge states from noise and a long one may lead to charge change destructively during readout. To make the balance, we actually made many measurements with various powers and durations, and finally chose the op-
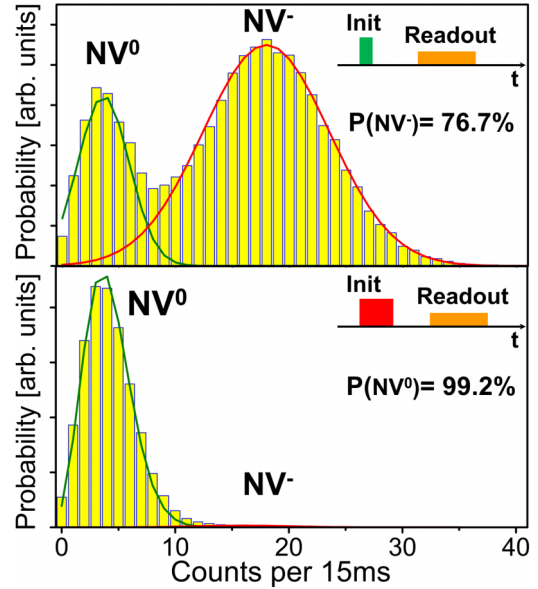

FIG. 2. The steady-state photon distributions of two charge states initialized with different lasers. In the top picture, the 532-nm pulse is 400 μW and 20 μs, which leads to $76.7 \pm 0.9\%$ population of NV^-. In the bottom one, the 637-nm pulse is 350 μW and 1 ms, which results in $99.2 \pm 1.8\%$ population of NV^0. In both cases, the weak 594-nm readout pulse has a power of 8 μW and lasts 15 ms. The solid lines are the fits to the data using two Poissonian distributions.

timal setting of 15 ms and 8 μW for our system. To improve the performance of the single-shot readout, multiple methods were applied to promote the signal-to-noise ratio radically, such as solid immersion lens [24,25], cryogenic condition [36], and machine learning [37,38]. With the help of a solid immersion lens around the NV center, the NV^- population can be increased to ~98% with single-shot readout [24,39], which is of importance for quantum computing and sensing.

To confirm that the switching back and forth between two charge states is a two-photon process, we measured how the NV^- population changes with laser power. As shown in Fig. 3(a), after the NV center is initialized to negative charge
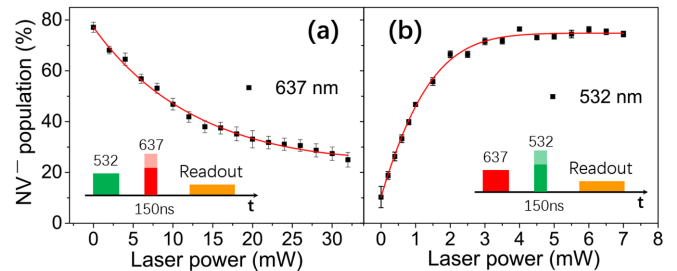

FIG. 3. Charge-state populations resulted from 532- and 637-nm lasers of different power. (a) The NV center is first initialized to NV^-, then a 637-nm pulse of 150 ns is used to ionize it. (b) Conversely, the NV is first prepared in NV^0, then a 532-nm pulse is used to convert it to negative charge. The 594-nm readout pulse for both cases are 15 ms and 8 μW. The data are fitted with Eq. (3), where $\gamma = \alpha I + \beta I^2$, which indicates a combination of linear and quadratic dependence on laser power.

by 532-nm laser, we applied a 637-nm pulse with variable power to ionize it, and then the remaining NV$^-$ population is measured. Considering the $\sim$200-ns lifetime of the singlet [37], we set the duration of the ionization pulse as 150 ns to avoid circular pumping. This setting is also applied to the neutral-to-negative experiment in Fig. 3(b) consistently to maintain comparability, where the time sequence is the same except for swapping the two lasers. The results show that the 532-nm laser can perform the recombination process with much less power than that needed for 637 nm acting on the ionization process, which means a higher conversion efficiency. To fit these data, we use the following simple rate equations describing the CSC model [40]:

$$\dot{P}^- = \gamma_r P^0 - \gamma_i P^-, \tag{1}$$

$$\dot{P}^0 = -\gamma_r P^0 + \gamma_i P^-. \tag{2}$$

Here P^- and P^0 are the populations of the two charge states and γ_r, γ_i are the recombination and ionization rates, respectively. Supposing the solution has the form $P^{-,0} = A + Be^{C\tau}$, it is easy to derive that

$$P^- = P^-_{\mathrm{st}} + (P^-_0 - P^-_{\mathrm{st}})e^{-\gamma\tau}, \tag{3}$$

where P^-_{st} is a steady-state NV$^-$ population and P^-_0 is the initial one. $\gamma = \gamma_i + \gamma_r$ represents the measured charge conversion rate in the experiment. Although the two-photon process for CSC indicates $\gamma \propto I^2$, we actually fit the data well using the formula $\gamma = \alpha I + \beta I^2$ [28]. The reason might be that there exists some saturation effect which causes the charge conversion rate to be linearly dependent on power partially.

III. INFRARED-ASSISTED CHARGE STATE CONVERSION

In fact, a blue photon with a wavelength less than 477 nm (corresponding to 2.6 eV, the energy gap between the triplet ground state and the conduction band) is more efficient in exciting the NV center than photons at other wavelengths since it can simplify the ionization and recombination of the charge state into a single-photon process due to its even higher energy than needed [41]. However, a single blue illumination tends to populate the NV center in the NV^0 charge state [22,28], not giving access to controlling both conversions. Instead, combining two colors of photons to excite the two transitions of the CSC process simultaneously may accelerate the conversion. Figure 4 displays the experimental result of combining 1040-nm and 532-nm (637-nm) light to illuminate the NV center after the charge is prepared in NV^0 (NV$^-$). The NV$^-$ population is measured as a function of laser duration and the data are also fitted with the function Eq. (3) except that γ is a to-be-measured constant now. The time sequences for the two experiments are shown together in Fig. 4(a). In Fig. 4(b), the recombination rate is estimated to be increased from about 0.17 μs^{-1} (under green excitation alone) to 0.7 μs^{-1} by the additional excitation with IR light of 5 mW and to about 1.93 μs^{-1} with 70 mW. Meanwhile, Fig. 4(c) shows that the ionization rate is increased from about 0.05 μs^{-1} (under red excitation alone) to 0.38 μs^{-1} with additional IR at 70 mW. In comparison, the 1040-nm illumination alone brings no change. Therefore, it is reasonable to consider
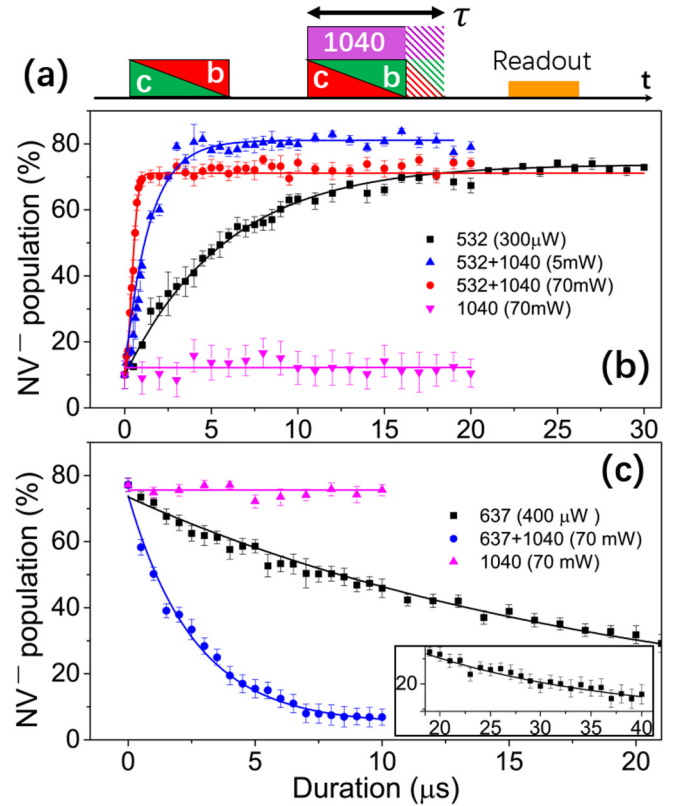

FIG. 4. Charge-state population dynamics of NV center under illumination by lasers of different colors and variable duration. (a) Pulse sequence for (b) and (c). Following a 10-μs initialization pulse, a second pulse of variable duration for charge conversion is applied with or without a 1040-nm pulse together, then a 8-μW yellow pulse lasting 15 ms is used to detect the NV$^-$ population. (b) Rising NV$^-$ population with longer laser pulse. The conversion process is greatly accelerated by the simultaneous excitation of 532-nm (300 μW) and IR light, but the steady-state populations are different for different IR powers (5 mW and 70 mW). The red pulse for initialization is 350 μW. (c) Accelerated charge conversion to NV^0 with longer pulse (637-nm laser, 400 μW; IR laser, 70 mW). The green initialization pulse is 300 μW. The inset displays the data above 20-μs duration when there is only 637-nm laser. Such an extended measurement is for accurate fitting to the data. For both cases, the 1040-nm pulse alone does not change the population. The solid lines are the fits to the data using Eq. (3).

that the IR illumination only pumps the second transition of the two-photon process, acting as an accelerator for the CSC. One photon of 1040 nm has an energy of 1.19 eV, which is larger than the energy gap 0.65 eV between the excited state and the conduction band of NV$^-$ [41], and should be also larger than the gap between the ground state and valence band of NV^0. Thus, other lasers of near-IR wavelengths such as 780 nm can certainly play the same accelerating role [19,30]. The difference is that the 1040-nm laser may not induce the stimulated emission as the 780 nm one does, which is also not observed in our experiment. It is because that the spontaneous fluorescence spectrum of NV center ends around 800 nm [31].

Another noteworthy thing in Fig. 4(b) is that the final steady-state population of NV$^-$ is further altered by the
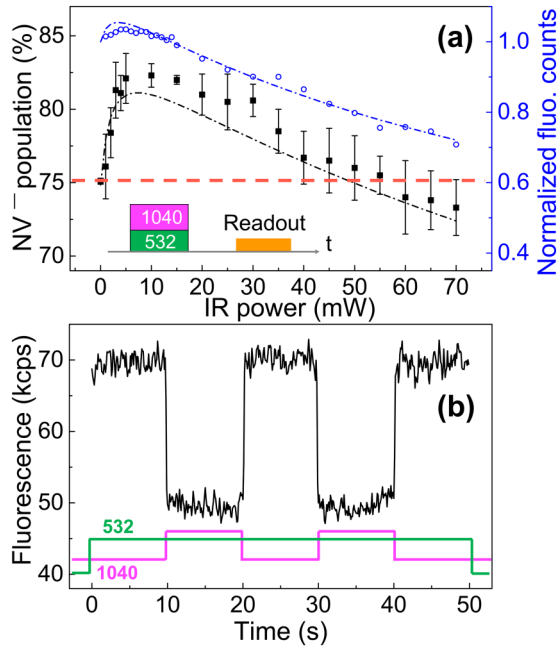
FIG. 5. The response relation of the charge population and fluorescence to IR power. (a) The NV$^-$ population (black squares) rises rapidly with the increase of IR power and reaches the top about 82% between 5 and 10 mW, then decreases slowly and become even lower than the initial value when above 55 mW (indicated by the pink dashed line). 532 nm: 400 μW, 10 μs; 1040 nm: 10 μs; 594 nm: 8 μW, 15 ms. (b) Modulated fluorescence under the simultaneous excitation of continuous green and gated IR laser. The power is 300 μW for green and 70 mW for IR. The gate time is 10 s. A series of such time traces are measured for different IR powers and the quenched fluorescence counts are normalized to when IR is off and plotted in (a) together, shown as blue circles. The dash-dot lines are fits to the data using the model in the Appendix.

existence of a 1040-nm laser. The population even reaches ~82% when the IR power is 5 mW, but drops to ~71% (the fluctuation of this number becomes large at long laser durations) when it is 70 mW, which is even slightly lower than when there is only green light (approaching 75%). To give a general knowledge about the relation, we measured the steady-state charge population as a function of IR power in Fig. 5(a). The NV$^-$ population rapidly reaches its highest about 82% as IR power increases to between 5 and 10 mW, and then decreases slowly, even arriving at below the initial value when the power rises above about 55 mW. This phenomenon of power-dependent enhancement and suppression results from the competition between the ionization and recombination processes induced by the simultaneous excitation with IR and green light.

Actually, this kind of effect is more straightforward in the observation of fluorescence, which can be modulated by switching on and off the IR laser while keeping the green excitation always on [42]. As shown in Fig. 5(b), the time trace of NV$^-$ fluorescence is quenched by about 30% once the 70-mW IR laser is on. We measured a series of modulated time traces by changing the IR power, and plot the data together in Fig. 5(a) (blue circles). When above 10 mW, a linearly decreasing power dependence on IR light of the fluorescence

counts is clearly shown, which indicates that the quenching contrast can be further enhanced by increasing IR power, although higher power cannot be provided by our laser device. When the IR light is below 10 mW, buried in the noise, the fluorescence can hardly present any change with the method of observing quenching contrast and the used timebin of 50 ms. Then, we turn to measure these data in another way, recording the nanosecond-timescale dynamical time trace of fluorescence with a self-made 50 ps-resolution time tagger based on a commercial field-programmable-gate-array (FPGA) module. The difference in the trace counts with and without IR light is now distinguishable and the data from 1 to 15 mW are remeasured and shown in Fig. 5(a). The fluorescence in the low-IR-power region shows a tiny growth and reaches the maximum of a 3.5% increase at 5 mW. Yet this is very small compared with the result in Ref. [31], where for a bulk diamond, the fluorescence is increased about 20% by a 10-mW IR laser, even observed on the ms-level timescale. According to the text, we speculate that the reason lies in the special fabrication of a shallow and dense NV layer ($10/\mu$m^2) in their sample, which might cause some ensemble effect or interplay between adjacent NVs even within the chosen small location.

Nevertheless, most of the previous works reported only suppression of fluorescence, no matter if it were in nanodiamonds [42,43] or in bulk NVs in a similar work (where IR enhancement is only observed in shallow NVs) [29]. To confirm whether this tiny growth is real, we built an eight-level rate equation model to simulate the data since the previous two-state equations are too simple to afford this job. For the description of the model, please see the Appendix. The predicted data are displayed in Fig. 5(a) (dash-dot lines), in good agreement with the experimental data for both NV$^-$ population and fluorescence counts. The slight deviation could be induced by various factors, such as sample type, NV location, local electromagnetic and strain environment, optical fluctuation, and so on, as well as the incompleteness of the model, which fails to involve other complex spin structures (phonon sidebands, for instance). Comparing the two experimental curves, the fluorescence counts basically present the same response trend to IR power as that of the steady-state NV$^-$ population, but its response rate is much weaker than that of NV$^-$ population when the power is below 5 mW. The reason could be that the IR laser drives the NV into a rapid dynamically balanced charge-changing process [23,44], in which the instantaneous NV$^-$ proportion is weakly increased, while the excited-state population that contributes to the fluorescence is saturated; on the other hand, the NV$^-$ population is measured in the steady state long after the lasers are off and can be enhanced a lot by IR, which is the balance result of the competition between the ionization and recombination processes. Above 10 mW, even the dynamical balance of the two charge states is shifted towards NV^0. This phenomenon indicates that it could be approximately equivalent to characterize the NV charge state by measuring fluorescence and NV population, especially for a shallower NV center which is measured in the steady state. If we look at Fig. 4(b) again, we could find that the green light alone changes the charge state little when the pulse is shorter than 500 ns. Hence, enough photons can be produced to characterize the charge population with a proper green pulse.
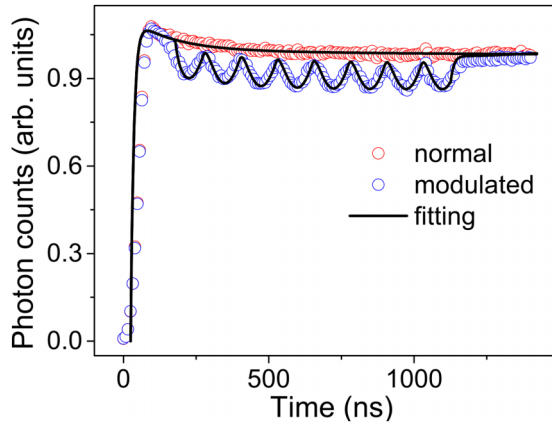
FIG. 6. Time-resolved fluorescence traces of spin state initialized to $m_s = 0$ with (blue circles, lower) and without (red circles, upper) fast sinusoidal modulation by IR light. The modulation lasts for 1000 ns and the period is 125 ns. IR power: 55 mW. The solid black lines are fits to the data with the same model and parameters as in the Appendix.

Finally, to see how fast the fluorescence time trace can be modulated by IR light, we give a sinusoidal modulated radio frequency (RF) signal to the acoustooptic modulator (AOM) for IR, while keeping the green light on. As shown in Fig. 6, when the RF amplitude modulation is 4 MHz, the time trace oscillates clearly with a period of 125 ns, which is reasonable due to $I(t) \propto \sin^2(\omega_M t) = [1 - \cos(2\omega_M t)]/2$, where ω_M is the modulation frequency. We also measured time traces at oscillation periods of 62.5 ns and 31.25 ns (data not shown). The time traces at 62.5 ns still show oscillation but a decrease in sinusoidal contrast, and the ones at 31.25 do not show oscillation, but instead a general fluorescence quench, which is due to the slow AOM rise time of 53 ns. Considering the rise or fall of the fluorescence takes only half of the period, this response to IR power looks fast. Since CSC is considered a slower process as discussed previously (~ 500 ns even with strong IR), it is hard to explain the modulation by CSC alone and imagine that the electron moves back and forth frequently just due to the discarding and recapturing of it to and from somewhere. Here, we might attribute the fluorescence oscillation partially to some IR-enhanced nonradiative transition, which possibly drives the electron into the singlet. Once the IR power is weaker, the population in the excited state is increased again under the continuous pumping of green light.

In summary, we experimentally demonstrated the fundamental dynamics of charge-state conversion between NV$^-$ and NV^0. Four typical wavelengths of their own colors are employed to manipulate it, and each color of light serves some kind of superiority over others in the process. We find that the charge conversion rate varies greatly at different laser powers and an additional excitation with IR light makes a striking difference in accelerating the conversion process. With this simultaneous excitation, we also find that the steady-state NV$^-$ population is increased when the IR power is below 55 mW, but reduced above that, reaching its highest about 82% between 5 and 10 mW. Meanwhile, the fluorescence counts basically follow the same dependence trend on IR power as the NV$^-$ population, but which is weak in the low

IR-power region. We also display the time-resolved fluorescence trace with fast sinusoidal modulation by IR light and attribute it partially to some IR-enhanced nonradiative transition. Our results clarify some conclusions of previous studies and lead to a clearer understanding of the NV charge state dynamics, which provides a solid foundation for our next-step work, such as the IR-assisted spin readout via spin-to-charge conversion and magnetic-field sensing.

APPENDIX

To predict the data strictly, we build an eight-level model to simulate the NV$^-$-NV^0 system, as depicted in Fig. 7. The rate equations are listed as follows:

$$\dot{P}_1 = -K_e^- P_1 + K_f^- P_3 + K_{61} P_6 + \tfrac{1}{2}(Kr_G + Kr_{IR})P_8,$$

$$\dot{P}_2 = -K_e^- P_2 + K_f^- P_4 + K_{62} P_6 + \tfrac{1}{2}(Kr_G + Kr_{IR})P_8,$$

$$\dot{P}_3 = -(K_f^- + K_{35} + Ki_G + Ki_{IR})P_3 + K_e^- P_1,$$

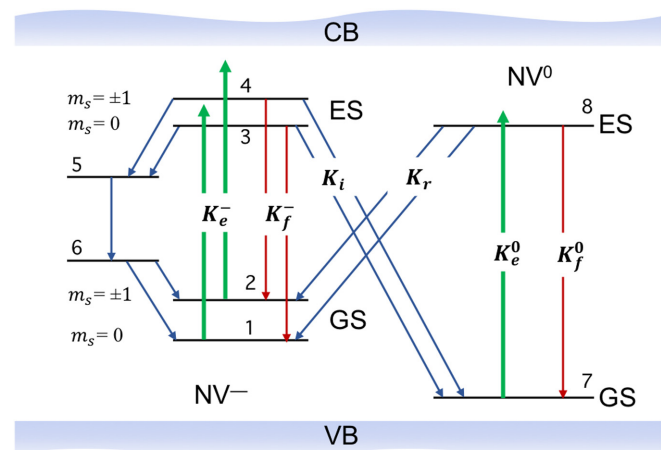$$\dot{P}_4 = -(K_f^- + K_{45} + Ki_G + Ki_{IR})P_4 + K_e^- P_2,$$

FIG. 7. Diagram of the energy levels and transitions between spins. The sublevels $m_s = 0$ and $m_s = \pm 1$ of the ground state (GS) are labeled 1 and 2, and that of the excited state (ES) are labeled 3 and 4. The excited and ground states of the singlet are labeled 5 and 6. The NV^0 is simplified to two levels and the GS and ES are labeled 7 and 8, respectively. All the transitions that are denoted as arrows are considered in the equations. 1040 nm is supposed to excite the transition in singlet, but the excitation rate is small and has little effect on our simulation, so it is ignored. K_e^- and K_e^0 are the green excitation rates for the two charges, while K_f^- and K_f^0 are the fluorescence rates. Ki is the ionization transition rate from NV$^-$ ES to NV^0 GS, and Kr is the recombination transition rate of the reverse conversion. VB, valence band; CB, conduction band.
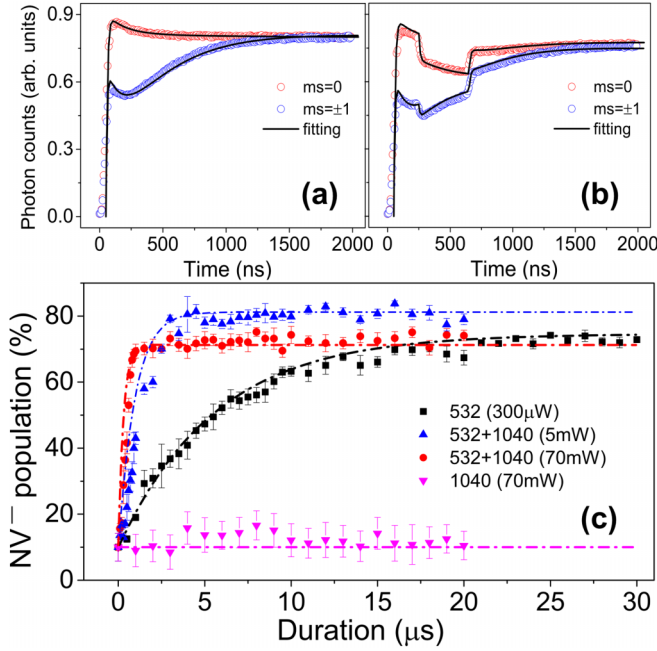
FIG. 8. Simulation for data with the eight-level model. (a) Dynamical fluorescence time traces of spin states initialized to $m_s = 0$ (red circles, upper) and $m_s = \pm 1$ (blue circles, lower). (b) Time traces with modulation by 30-mW IR light for 400 ns. The solid black lines are fits to the data. (c) New fits to the data in Fig. 4(b) with the model, denoted with dash-dotted lines.

$$\dot{P}_5 = -K_{56}P_5 + K_{35}P_3 + K_{45}P_4,$$
$$\dot{P}_6 = -(K_{61} + K_{62})P_6 + K_{56}P_5,$$
$$\dot{P}_7 = -K_e^0 P_7 + K_f^0 P_8 + (Ki_G + Ki_{IR})(P_3 + P_4),$$
$$\dot{P}_8 = -(K_f^0 + Kr_G + Kr_{IR})P_8 + K_e^0 P_7.$$

Here P_n ($n \in [1,8]$) denotes the population on level n, K_{ij} denotes the transition rate from levels i to j. The ionization transition rate Ki includes the effects of both green and IR light ($Ki = Ki_G + Ki_{IR}$), as does the recombination transition rate ($Kr = Kr_G + Kr_{IR}$). But Kr is assumed to be split equally for spin $m_s = 0$ and $m_s = \pm 1$ of NV$^-$ GS.

To solve the equations, the power-independent transition rates are determined carefully according to Refs. [29,45]. As for the six power-dependent rates, K_e^-, K_e^0, Ki_G, Kr_G, Ki_{IR}, Kr_{IR} since they could differ a lot from existing literature due to the different experimental setup and optical efficiency, we obtain them by fitting the dynamical fluorescence time traces

TABLE I. Spin transition rates used for numerical simulation in NV center.

Transition	Rate	Transition	rate
K_f^-	77 μs^{-1}	K_e^-	27 μs^{-1}/mW
K_f^0	53 μs^{-1}	K_e^0	18 μs^{-1}/mW
K_{35}	7.9 μs^{-1}	Ki_G	4.9 μs^{-1}/mW
K_{45}	45 μs^{-1}	Kr_G	12 μs^{-1}/mW
K_{56}	1000 μs^{-1}	Ki_{IR}	0.6 μs^{-1}/mW
K_{61}	6.5 μs^{-1}	Kr_{IR}	3.1 μs^{-1}/mW
K_{62}	0.1 μs^{-1}		

of spin states initialized to $m_s = 0$ and $m_s = \pm 1$ (as shown in Fig. 8), which are recorded with a self-made 50-ps-resolution time tagger based on a commercial FPGA module. The rates Ki_{IR} and Kr_{IR} are obtained by adding the IR laser as a modulation [Fig. 8(b)]. From these nice fits, we successfully extracted all the transition rates between spins, and list them in Table I.

However, during the simulation of these time traces, we find that the predicted result is insensitive to some transition rates, even if you change them significantly. To make sure that the extracted transition rates are optimal and generally applicable, we actually optimize them by fitting the data in Figs. 4 and 5(a) simultaneously, which takes a lot of effort. The repredicted data for Fig. 4(b), as an example, is displayed in Fig. 8(c), which is also in good agreement with the experimental data. Therefore, we believe that we built a reasonable model which proves that the measured data are reliable.

Although we were not able to involve all the information of NV center, such as depth and density (single in our case), in the model, the several power-dependent transition rates are extracted from real experimental data with our setup, in which this information could be actually implicit to some extent. In any case, the transition rates still cannot lead to accurate prediction for every figure since the data points for the extraction of the rates can differ from one measurement to another due to various factors that induce fluctuations. For example, for the deviation between data and the fitted curve in Fig. 5(a), it is true that we can fix it using a special set of transition rates, but these rates will distort the predicted curves in the other figures significantly. We have to find the balance. In this sense, we can only say that our transition rates reflect an average effect over all the factors in the internal and external environments of the NV center.

[1] D. D. Awschalom, L. C. Bassett, A. S. Dzurak, E. L. Hu, and J. R. Petta, Science **339**, 1174 (2013).

[2] V. A. Norman, S. Majety, Z. Wang, W. H. Casey, N. Curro, and M. Radulaski, Infomat **3**, 869 (2021).

[3] I. Aharonovich, D. Englund, and M. Toth, Nat. Photon. **10**, 631 (2016).

[4] P. Qian, Z. Gu, R. Cao, R. Wen, Z. Y. Ou, J. F. Chen, and W. Zhang, Phys. Rev. Lett. **117**, 013602 (2016).

[5] P. Qian, Z. Gu, R, Wen, W. Zhang, and J. F. Chen, Phys. Rev. A **97**, 013806 (2018).

[6] I. Aharonovich and E. Neu, Adv. Opt. Mater. **2**, 911 (2014).

[7] S. Castelletto, B. Johnson, V. Ivády, N. Stavrias, T. Umeda, A. Gali, and T. Ohshima, Nat. Mater. **13**, 151 (2014).

[8] J.-F. Wang, Q. Li, F.-F. Yan, H. Liu, G.-P. Guo, W.-P. Zhang, X. Zhou, L.-P. Guo, Z.-H. Lin, J.-M. Cui et al., ACS Photon. **6**, 1736 (2019).

[9] T. T. Tran, K. Bray, M. J. Ford, M. Toth, and I. Aharonovich, Nat. Nanotechnol. **11**, 37 (2016).

[10] J. D. Caldwell, I. Aharonovich, G. Cassabois, J. H. Edgar, B. Gil, and D. Basov, Nat. Rev. Mater. **4**, 552 (2019).

[11] M. W. Doherty, N. B. Manson, P. Delaney, F. Jelezko, J. Wrachtrup, and L. C. Hollenberg, Phys. Rep. **528**, 1 (2013).

[12] J. Geng, Y. Wu, X. Wang, K. Xu, F. Shi, Y. Xie, X. Rong, and J. Du, Phys. Rev. Lett. **117**, 170501 (2016).

[13] B. Chen, J. Geng, F. Zhou, L. Song, H. Shen, and N. Xu, Appl. Phys. Lett. **114**, 041102 (2019).

[14] D. Suter and F. Jelezko, Prog. Nucl. Magn. Reson. Spectrosc. **98-99**, 50 (2017).

[15] Y. Song, Y. Tian, Z. Hu, F. Zhou, T. Xing, D. Lu, B. Chen, Y. Wang, N. Xu, and J. Du, Photon. Res. **8**, 1289 (2020).

[16] J. F. Barry, J. M. Schloss, E. Bauch, M. J. Turner, C. A. Hart, L. M. Pham, and R. L. Walsworth, Rev. Mod. Phys. **92**, 015004 (2020).

[17] T. Gaebel, M. Domhan, C. Wittmann, I. Popa, F. Jelezko, J. Rabeau, A. Greentree, S. Prawer, E. Trajkov, P. R. Hemmer *et al.*, Appl. Phys. B **82**, 243 (2006).

[18] K. Y. Han, S. K. Kim, C. Eggeling, and S. W. Hell, Nano Lett. **10**, 3199 (2010).

[19] X.-D. Chen, S. Li, A. Shen, Y. Dong, C.-H. Dong, G.-C. Guo, and F.-W. Sun, Phys. Rev. Applied **7**, 014008 (2017).

[20] E. Bourgeois, A. Jarmola, P. Siyushev, M. Gulka, J. Hruby, F. Jelezko, D. Budker, and M. Nesladek, Nat. Commun. **6**, 8577 (2015).

[21] P. Siyushev, M. Nesladek, E. Bourgeois, M. Gulka, J. Hruby, T. Yamamoto, M. Trupke, T. Teraji, J. Isoya, and F. Jelezko, Science **363**, 728 (2019).

[22] S. Dhomkar, J. Henshaw, H. Jayakumar, and C. A. Meriles, Sci. Adv. **2**, e1600911 (2016).

[23] H. Jayakumar, A. Lozovoi, D. Daw, and C. A. Meriles, Phys. Rev. Lett. **125**, 236601 (2020).

[24] B. J. Shields, Q. P. Unterreithmeier, N. P. de Leon, H. Park, and M. D. Lukin, Phys. Rev. Lett. **114**, 136402 (2015).

[25] D. A. Hopper, R. R. Grote, A. L. Exarhos, and L. C. Bassett, Phys. Rev. B **94**, 241201(R) (2016).

[26] P. Rembold, N. Oshnik, M. M. Müller, S. Montangero, T. Calarco, and E. Neu, AVS Quantum Sci. **2**, 024701 (2020).

[27] S. Pezzagna and J. Meijer, Appl. Phys. Rev. **8**, 011308 (2021).

[28] N. Aslam, G. Waldherr, P. Neumann, F. Jelezko, and J. Wrachtrup, New J. Phys. **15**, 013064 (2013).

[29] I. Meirzada, Y. Hovav, S. A. Wolf, and N. Bar-Gill, Phys. Rev. B **98**, 245411 (2018).

[30] L. Hacquebard and L. Childress, Phys. Rev. A **97**, 063408 (2018).

[31] P. Ji and M. Gurudev Dutt, Phys. Rev. B **94**, 024101 (2016).

[32] B. Chen, X. Hou, F. Ge, X. Zhang, Y. Ji, H. Li, P. Qian, Y. Wang, N. Xu, and J. Du, Nano Lett. **20**, 8267 (2020).

[33] P. Siyushev, H. Pinto, M. Vörös, A. Gali, F. Jelezko, and J. Wrachtrup, Phys. Rev. Lett. **110**, 167402 (2013).

[34] G. Waldherr, P. Neumann, S. F. Huelga, F. Jelezko, and J. Wrachtrup, Phys. Rev. Lett. **107**, 090401 (2011).

[35] D. M. Irber, F. Poggiali, F. Kong, M. Kieschnick, T. Lühmann, D. Kwiatkowski, J. Meijer, J. Du, F. Shi, and F. Reinhard, Nat. Commun. **12**, 532 (2021).

[36] Q. Zhang, Y. Guo, W. Ji, M. Wang, J. Yin, F. Kong, Y. Lin, C. Yin, F. Shi, Y. Wang *et al.*, Nat. Commun. **12**, 1 (2021).

[37] P. Qian, X. Lin, F. Zhou, R. Ye, Y. Ji, B. Chen, G. Xie, and N. Xu, Appl. Phys. Lett. **118**, 084001 (2021).

[38] G. Liu, M. Chen, Y.-X. Liu, D. Layden, and P. Cappellaro, Mach. Learn. Sci. Tech. **1**, 015003 (2020).

[39] T. Xie, Z. Zhao, X. Kong, W. Ma, M. Wang, X. Ye, P. Yu, Z. Yang, S. Xu, P. Wang *et al.*, Sci. Adv. **7**, eabg9204 (2021).

[40] X. Chen, C. Zou, Z. Gong, C. Dong, G. Guo, and F. Sun, Light Sci. Appl. **4**, e230 (2015).

[41] I. Meirzada, S. A. Wolf, and N. Bar-Gill, Phys. Rev. B **104**, 155413 (2021).

[42] M. Geiselmann, R. Marty, F. J. G. De Abajo, and R. Quidant, Nat. Phys. **9**, 785 (2013).

[43] N. D. Lai, O. Faklaris, D. Zheng, V. Jacques, H. Chang, J. Roch, and F. Treussart, New J. Phys. **15**, 033030 (2013).

[44] A. Lozovoi, H. Jayakumar, D. Daw, G. Vizkelethy, E. Bielejec, M. W. Doherty, J. Flick, and C. A. Meriles, Nat. Electron. **4**, 717 (2021).

[45] L. Robledo, H. Bernien, T. Van Der Sar, and R. Hanson, New J. Phys. **13**, 025013 (2011).